ADVANCED MATERIALS
www.advmat.de

Achieving Ultrahigh n-Type Thermoelectric Power Factor in an Intrinsically Large Transport-Fermi Energy Gap Conjugated Polymer

Jingyi Wang, Chengwen Wu, Zhibo Ren, Shuang-Yan Tian, Qianyu Ding, Xiran Pan, Xin-Yu Deng, Jupeng Chen, Jiatong Li, Juanrong Wang, Chen-Kai Pan, Kai Liu, Jia Zhu, Zhi Zhang, and Ting Lei**

The conductivity of organic thermoelectric materials has seen significant improvements in the past few years, but often at the expense of the Seebeck coefficient. Consequently, the thermoelectric performance, especially for n-type materials, remains considerably lower than that of their inorganic counterparts. Herein, a high-performance n-type thermoelectric polymer, P(TDPP-BT-LEG) is reported, with an unexpectedly high Seebeck coefficient and ultrahigh power factor, driven by its intrinsically large energy gap between the Fermi and transport energy levels and high charge carrier mobility. Notably, it is shown that strong electrostatic interactions induced by the ethylene glycol side chains facilitate charge transfer between the dopants and the polymer. This enables effective doping of polymers with high LUMO levels. Furthermore, efficient charge transport, arising from favorable molecular packing, allows the polymer to maintain high electrical conductivity even at low charge carrier concentrations. Ultimately, this polymer achieves a record-high n-type power factor of 397 μW m^{-1} K^{-2}, with a high Seebeck coefficient of −420 μV K^{-1}. This study highlights the potential of enhancing the Seebeck coefficient through precise energy level tuning and molecular design, fundamentally advancing the rational design of high-performance organic thermoelectric materials.

1. Introduction

Organic thermoelectric (OTE) materials have recently garnered increasing attention for their potential applications in body heat harvesting and wearable cooling, due to their lightweight, flexibility, and low toxicity.[1] The thermoelectric performance is typically evaluated using the figure of merit, $ZT = \sigma S^2 T/\kappa$, where S, σ, κ, and T represent the Seebeck coefficient, electrical conductivity, thermal conductivity, and absolute temperature, respectively. Additionally, the power factor (PF) $= \sigma S^2$ is also used, as high PF is important for high-power generation applications.[2] Over the past decade, research has focused on improving the electrical conductivity of OTE materials, which are known to exhibit characteristically low conductivity.[3] To date, several p-type and a limited number of n-type OTE materials have achieved electrical conductivity over 100 S cm^{-1}, with some even surpassing 1000 S cm^{-1} through careful

J. Wang, C. Wu, Z. Ren, S.-Y. Tian, Q. Ding, X. Pan, X.-Y. Deng, J. Chen, J. Li, J. Wang, Z. Zhang, T. Lei
National Key Laboratory of Advanced Micro and Nano Manufacture Technology
Key Laboratory of Polymer Chemistry and Physics of Ministry of Education
School of Materials Science and Engineering
Peking University
Beijing 100871, P. R. China
E-mail: zhizhang@pku.edu.cn; tinglei@pku.edu.cn

C.-K. Pan
Beijing National Laboratory for Molecular Sciences (BNLMS)
Key Laboratory of Polymer Chemistry and Physics of Ministry of Education
Center of Soft Matter Science and Engineering
College of Chemistry and Molecular Engineering
Peking University
Beijing 100871, P. R. China

K. Liu
Key Laboratory of Rubber-Plastics
Ministry of Education/Shandong Provincial Key Laboratory of Rubber-Plastics
Qingdao University of Science and Technology
Qingdao, Shandong 266042, P. R. China

Q. Ding, J. Zhu
Laboratory of Theoretical and Computational Nanoscience
CAS Center for Excellence in Nanoscience
National Center for Nanoscience and Technology
Chinese Academy of Sciences
Beijing 100190, P. R. China

The ORCID identification number(s) for the author(s) of this article can be found under https://doi.org/10.1002/adma.202512453

DOI: 10.1002/adma.202512453

molecular design and efficient doping.[3–7] However, while S is another critical, or even more important, parameter affecting the performance due to its quadratic relationship, less attention and effective strategies have been reported for its optimization.

State-of-the-art flexible/ductile inorganic thermoelectric materials (e.g., Ag_2Se, Bi_2Te_3-based systems) achieve concurrent high performance: S >100 μV K^{-1} at $\sigma \approx 1000$ S cm^{-1}, yielding PF >1000 μW m^{-1} K^{-2} and room-temperature ZT value > 0.4.[8–10] However, the S of OTE materials is typically only tens of μV K^{-1} after heavily doped, resulting in PF generally below 200 μW m^{-1} K^{-2} and ZT value under 0.1.[3] Previous studies have demonstrated that the S, which governs the energy transport properties of OTE materials, depends on the energy difference between the Fermi energy (E_F) and the transport energy (E_{Tr}):[11,12]

$$S = \frac{k_B}{q}\left[\frac{E_{Tr} - E_F}{k_B T} + A\right] \quad (1)$$

where E_F is affected by the charge carrier concentration, while the E_{Tr} is defined by the shape and position of the density of states (DOS).[13] De-doping reduces charge carrier concentration, shifting the E_F away from the E_{Tr}. This enhances the S while reducing σ, making the approach particularly effective for high-conductivity systems like the benchmark p-type thermoelectric material poly(3,4-ethylenedioxythiophene) (PEDOT).[14] Consequently, researchers pursue OTE materials with high charge carrier mobilities to overcome the S-σ trade-off relationship.[15] In addition, some other strategies have also been explored to engineer the DOS of p-type OTE materials, such as blending polymers with distinct energy levels, inducing bimodal molecular orientations, or incorporating small conjugated molecules to trigger energy splitting.[14,16,17] These approaches can decouple the E_F from the E_{Tr}, thereby enhancing the S. Furthermore, inspired by the energy filtering effect in inorganic materials, ionic liquids or zwitterionic molecules are employed to scatter low-energy charge carriers through strong ionic dipoles in p-type polymers.[18,19] This process increases the average transport energy of the charge carriers, thereby enhancing the S without significantly degrading σ. However, to date, molecular design strategies, particularly for n-type materials, that could enable high S are still unknown and less explored.

At present, E_{Tr}, a hypothetical transport energy level, remains experimentally challenging to precisely determine.[20] Studies indicate, however, that this transport energy level correlates with frontier orbitals—specifically, the highest occupied molecular orbital (HOMO) of p-type materials and the lowest unoccupied molecular orbital (LUMO) of n-type materials.[11,21] Here, we investigated several n-type conjugated polymers with varying LUMO levels and observed that the polymer P(TDPP-BT-LEG), featuring ethylene glycol (EG) side chains and a higher LUMO level, exhibited an exceptionally high S. We propose that its high LUMO level elevates the E_{Tr} and creates a substantially large gap between the E_F and the E_{Tr}. Through molecular dynamics simulations, we demonstrated that EG side chains significantly enhance electrostatic interactions between dopants and conjugated polymers, ensuring enhanced charge transfer and efficient doping in high-LUMO-level polymers. Meanwhile, efficient interchain charge transport via 2,1,3-benzothiadiazole (BT)-BT coupling enhances the charge carrier transport and σ of P(TDPP-BT-LEG). All these factors synergistically contribute to a maximum PF value of 397 μW m^{-1} K^{-2}, with a corresponding ZT value of 0.19, which are among the highest in n-type OTE polymers.

2. Results and Discussion

2.1. Polymer Design, Synthesis, and Characterization

We selected diketopyrrolopyrrole (DPP)-based conjugated polymers for investigation (**Figure 1a**), as these polymers exhibit tunable energy levels and high backbone planarity, both of which are conducive to achieving high charge carrier mobility and conductivity.[22,23] We grafted these polymers with various side chains, including linear ethylene glycol (LEG) and branched ethylene glycol (BEG) side chains, as well as branched alkyl (C8C10) side chains for a more detailed comparison. Linear alkyl side-chain polymers, which exhibit poor solubility, were not studied further. Polymers functionalized with LEG and BEG side chains were prepared under similar reaction conditions (Figure 1b). First, the side chains were introduced onto TDPP using potassium carbonate in N,N-Dimethylformamide (DMF). Subsequently, the resulting intermediate was converted into a distannylated compound under low-temperature, strongly basic conditions. Finally, all polymers were obtained via Pd-catalyzed Stille coupling reactions, purified by Soxhlet extraction, and collected in chloroform. Polymers featuring C8C10 side chains were prepared following the reported method.[23] Detailed synthesis procedures were provided in the Supporting Information.

The density functional theory (DFT)-calculated energy levels of the trimeric oligomers of TDPP-BT, TDPP-BT2F, and TDPP-TQ are shown in **Figure 2a**. Their LUMO level decreases progressively across the series. We validated the LUMO level of these polymers using cyclic voltammetry (CV), confirming consistency with the computational predictions (Figure 2b; Figure S1 and Table S1, Supporting Information). Polymers with EG side chains display a lower LUMO level, which corresponds to a higher electron affinity, compared to their alkyl-side-chain analogues, as indicated by CV tests. This is unexpected, since conventional wisdom thinks that the side chains should not affect the energy levels. We will demonstrate later that that effect is due to the EG side chain-assisted n-doping. UV–vis-NIR spectra revealed that TDPP-TQ polymers display a pronounced redshift in absorption maxima and a narrower bandgap compared to TDPP-BT and TDPP-BT2F polymers (Figure 2c; Figure S2, Supporting Information), attributable to the strong quinoidal property of the TQ moiety.[23] We utilized n-dopant (4-(1,3-dimethyl-2,3-dihydro-1H-benzoimidazol-2-yl) phenyl) dimethylamine (*N*-DMBI) for n-doping (Figure 1a). After *N*-DMBI doping, polymers with EG side chains displayed two characteristic (bi)polaron absorption bands in the near-infrared region (Figure 2d–f). As the polymer LUMO level decreases from BT to TQ, the intensification of (bi)polaron peak becomes more pronounced, indicating enhanced doping efficiency. Among alkyl-side-chain analogues, only P(TDPP-TQ-C8C10) exhibited effective n-doping in UV–vis-NIR absorption spectra—albeit requiring higher dopant ratios—whereas P(TDPP-BT-C8C10) and P(TDPP-BT2F-C8C10) showed no discernible (bi)polaron signatures (Figure S2, Supporting Information). XPS also showed that doped

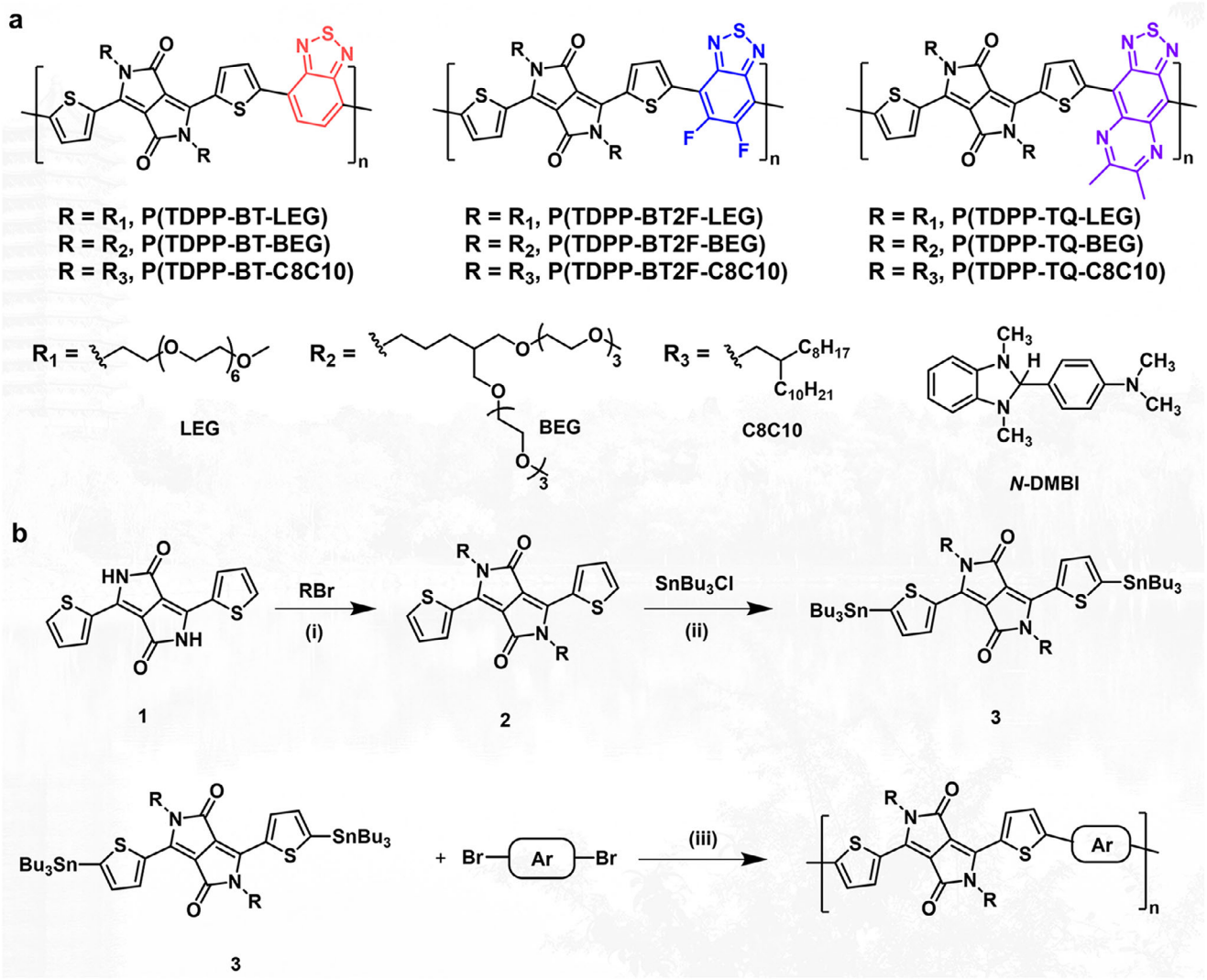

Figure 1. a) Chemical structures of DPP-based conjugated polymers and the n-dopant *N*-DMBI. b) Synthesis of six polymers with EG side chains. Reagents and conditions: i) K_2CO_3, DMF, 110 °C, 12 h; ii) LDA, THF, −110 °C to −78 °C, 2 h; iii) $Pd(PPh_3)_4$, *o*-xylene, 140 °C, 48 h. Compound 2 was synthesized according to our previous work.[24]

P(TDPP-BT-C8C10) has weaker *N*-DMBI$^+$ signals than doped P(TDPP-BT-LEG) at the same doping ratio (Figure S3, Supporting Information). The above results suggest that EG side chains greatly enhance the n-doping efficiency in these n-type polymers.

The thermoelectric (TE) performances of the nine polymers are summarized in **Table 1**. Polymers bearing EG side chains achieve the optimal thermoelectric performances at low doping concentrations, with the LEG variants outperforming their BEG counterparts (Figure 2g–i; Figures S4–S7, Supporting Information). We observed that lower polymer LUMO levels correlate with higher maximum σ after doping, albeit with diminished S — a trend independent of side-chain architecture. Among alkyl-side-chain polymers, only P(TDPP-TQ-C8C10) exhibited measurable σ under heavy *N*-DMBI doping, consistent with spectroscopic evidence (Figure S8, Supporting Information). Meanwhile, P(TDPP-TQ-C8C10) exhibited lower thermoelectric performance than P(TDPP-TQ-LEG). Notably, P(TDPP-BT-LEG) achieved a record-high *PF* of 397 μW m^{-1} K^{-2} at 15 mol% *N*-DMBI doping, with a high S of −420 μV K^{-1} and relatively high σ of 22.5 S cm^{-1}. The stable, time-independent thermoelectric voltage discards the ionic contributions to the high S (Figure S9, Supporting Information). The κ of P(TDPP-BT-LEG) was measured using an in-plane 3-omega method. After conductivity correction, the κ value is estimated to be 0.62 ± 0.05 W m^{-1} K^{-1}, and therefore, the *ZT* value of P(TDPP-BT-LEG) is calculated to be 0.19 ± 0.02. Alternatively, another n-dopant, tetrakis(dimethylamino)ethylene (TDAE), also effectively doped EG-side-chain polymers (Figure S10, Supporting Information). Under TDAE doping, P(TDPP-BT-LEG) similarly exhibited higher S than other polymers, but with a decreased TE performance than the *N*-DMBI-doped one.

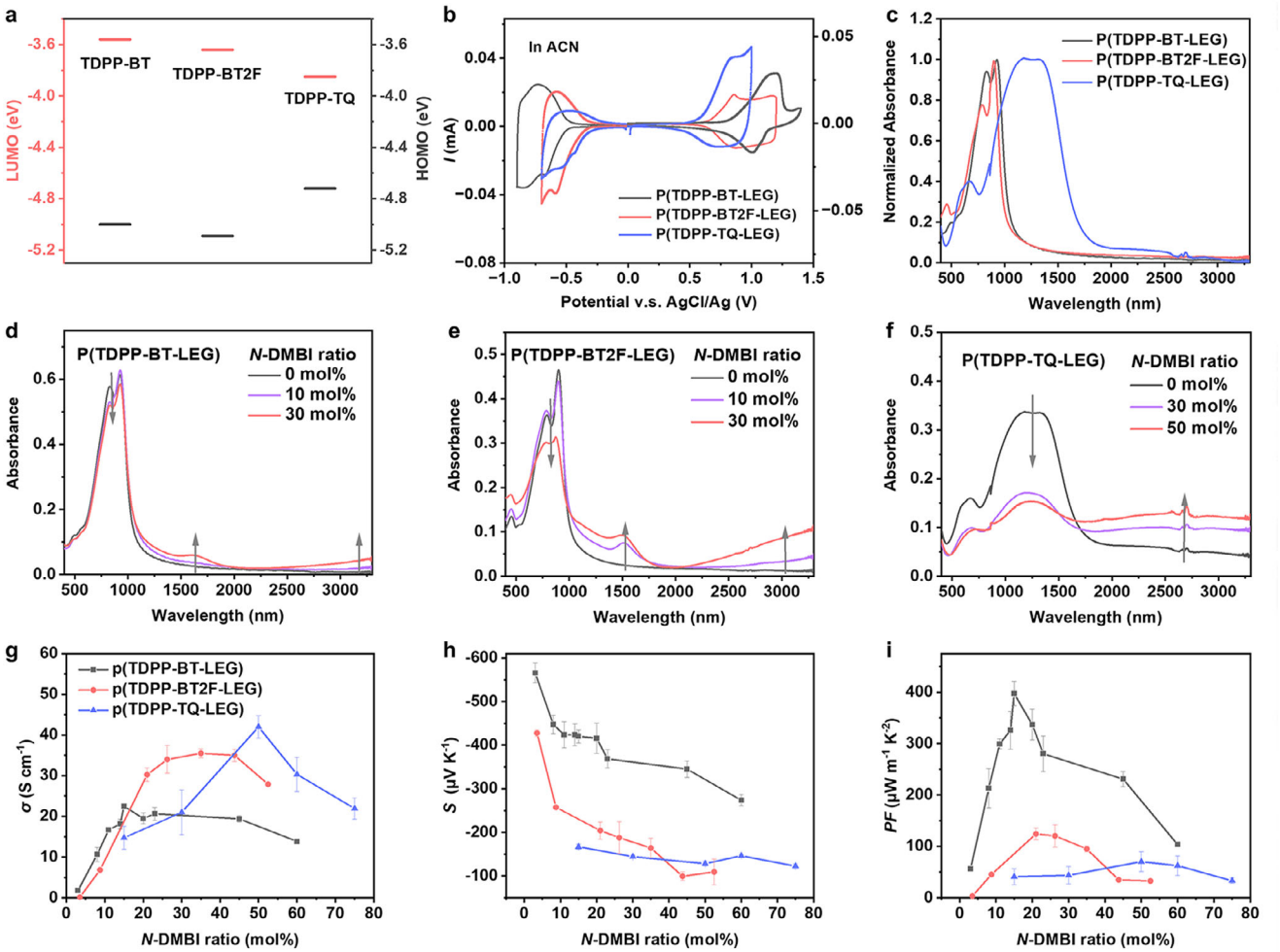

Figure 2. a) Calculated energy levels of the trimeric oligomers representing the three conjugated backbones (side chains replaced with methyl groups for simplicity). b) Cyclic voltammograms of the LEG-side-chain polymers in acetonitrile. c) UV–vis-NIR absorption spectra of pristine films of P(TDPP-BT-LEG), P(TDPP-BT2F-LEG), and P(TDPP-TQ-LEG). d–f) UV–vis-NIR absorption spectra of P(TDPP-BT-LEG), P(TDPP-BT2F-LEG), and P(TDPP-TQ-LEG) films at varying *N*-DMBI doping ratios. g–i) Doping concentration dependence of (g) σ, (h) *S*, and (i) *PF* for the *N*-DMBI doped LEG-side-chain polymer films.

Table 1. Thermoelectric performance comparison for the nine thermoelectric polymers.

Materials	LUMO[a)] [eV]	σ_{max} [S cm^{-1}]	PF_{max} [μW m^{-1} K^{-2}]	Seebeck @PF_{max} [μV K^{-1}]	σ@PF_{max} [S cm^{-1}]
P(TDPP-BT-LEG)	−3.83	23.6	397(± 24)	−420(± 15)	22.3(± 0.3)
P(TDPP-BT2F-LEG)	−3.95	37.4	124(± 11)	−204(± 20)	30.2(± 1.6)
P(TDPP-TQ-LEG)	−4.01	44.8	70(± 19)	−128(± 10)	42.0(± 2.8)
P(TDPP-BT-BEG)	−3.78	5.6	65(± 13)	−320(± 17)	4.0(± 1.3)
P(TDPP-BT2F-BEG)	−3.92	7.6	58(± 7)	−285(± 15)	5.8(± 0.2)
P(TDPP-TQ-BEG)	−4.03	16.8	64(± 13)	−214(± 20)	15.9(± 1.9)
P(TDPP-BT-C8C10)	−3.55	–	–	–	–
P(TDPP-BT2F-C8C10)	−3.56	–	–	–	–
P(TDPP-TQ-C8C10)	−3.86	15.9	64(± 7)	−201(± 11)	15.7(± 0.2)

[a)] Measured by cyclic voltammograms.

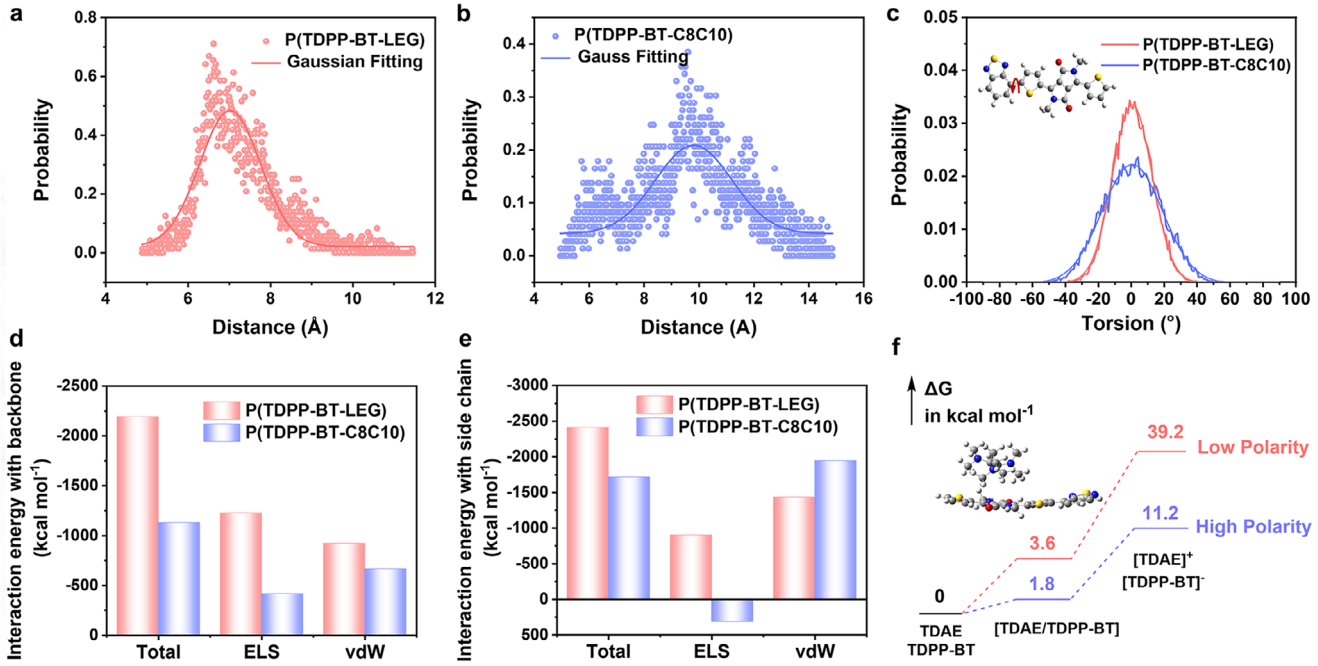

Figure 3. Spatial distribution of *N*-DMBI$^+$ around polymer backbone in a) P(TDPP-BT-LEG) and b) P(TDPP-BT-C8C10) extracted from MD simulations. c) Torsion angle distribution for the T-BT dihedral in both systems. d) Interaction energies between *N*-DMBI$^+$ and polymer backbones. Negative values denote attractive interactions. P(TDPP-BT-LEG) exhibits stronger total interactions (Total), including electrostatic (ELS) and van der Waals interactions (vdW), than P(TDPP-BT-C8C10). e) Interaction energies between *N*-DMBI$^+$ and polymer side chains. Positive ELS values indicate repulsive interaction. f) Gibbs free energy change (ΔG) for charge transfer in simulated solvent environments.

2.2. Electrostatic Interactions Enhanced n-doping

We further explored the impact of side-chain chemistry on doping behavior, specifically addressing why polymers featuring EG side chains demonstrated enhanced reductive susceptibility relative to alkyl-side-chain analogues. Previous studies indicated that EG side chains enhance polymer-dopant miscibility, thus improving doping efficiency and conductivity.[25,26] However, our experimental results demonstrated that P(TDPP-BT-C8C10) and P(TDPP-BT2F-C8C10) exhibited no detectable conductivity even at elevated dopant concentrations. Doping fundamentally depends on intermolecular charge transfer between organic semiconductors and dopants, a process governed by molecular energy level alignment and electrostatic (ELS) interactions among ionized species.[27] Xu et al. have established that the electron affinity of organic semiconductors must be higher than 3.8 eV for effective doping by *N*-DMBI.[28] Note that the electron affinity of the backbones of TDPP-BT (3.62 eV) and TDPP-BT2F (3.70 eV) is higher than the threshold (Table S2, Supporting Information). We speculate that the doping disparities are attributed to side-chain-induced variations in electrostatic interactions.

The electrostatic interactions between charged dopants and TDPP-BT polymers featuring LEG and C8C10 side chains were explored using molecular dynamics (MD) simulation (see Supplementary Information for more details).[29] During the simulation, we noticed that LEG side chains provided sufficient space for dopant diffusion, enabling higher dopant loading densities that effectively interact with conjugated backbones (Figure S11, Supporting Information).[30,31] After a consecutive 1 ns room-temperature MD simulation, we analyzed the spatial distribution of *N*-DMBI$^+$ around the backbones in both systems during the last 200 ps (**Figure 3**a,b; Figures S12 and S13, Supporting Information). The results indicated a more confined spatial distribution of *N*-DMBI$^+$ in the P(TDPP-BT-LEG) system, exhibiting a most probable distance of 7.0 Å to the polymer backbone. In contrast, the distribution is broader in P(TDPP-BT-C8C10), with a peak distance of 9.8 Å. We subsequently extracted torsion angle distributions of T-DPP and T-BT dihedral angles for investigating polymer conformations (Figure 3c; Figure S14, Supporting Information). P(TDPP-BT-LEG) exhibits narrower torsion angle distributions for both dihedral angles, with full width at half maximum (FWHM) recorded at 16.38° for T-DPP and 24.0° for T-BT. Whereas P(TDPP-BT-C8C10) displays broader distributions: 21.6° for T-DPP and 36.9° for T-BT. These observations suggest that the polymer with LEG side chain possesses enhanced interactions with *N*-DMBI$^+$ and reduced conformational disorder compared to its branched alkyl chain counterparts, thereby facilitating charge transport with increased σ.[29] Similarly, the lower thermoelectric performance of polymers with BEG side chains can be attributed to an increase in structural disorder. Additionally, polymers with BEG side chains also have a larger π–π stacking distance, which impedes interchain charge transport (Table S3, Supporting Information).

We analyzed non-covalent interactions, including electrostatic (ELS) and van der Waals (vdW) interactions, in different systems using energy decomposition analysis (EDA) based on the force field (Figure 3d,e; Table S4, Supporting Information).[32,33] A larger negative energy denotes a stronger attractive interaction. The dopant cations and polymers exhibited stronger

interactions in the P(TDPP-BT-LEG) system, almost twice compared with that in the P(TDPP-BT-C8C10) system (−2195 kcal mol^{-1} vs −1195 kcal mol^{-1}). The ELS interactions between *N*-DMBI$^+$ and the polymer backbone, as well as between *N*-DMBI$^+$ and the side chains, showed notably strong negative values of −1228 and −901 kcal mol^{-1}, respectively, which favor the stabilization of dopant cations and promote charge transfer. The strong and balanced ELS interactions facilitate the generation and transport of free charge carriers, either by Coulomb trap overlap or through the electric screening effect, which reduces the trap height.[29,34] In contrast, the P(TDPP-BT-C8C10) system exhibited significantly weaker ELS interaction: the *N*-DMBI$^+$-backbone interaction is only one-third the magnitude of that in P(TDPP-BT-LEG), while the *N*-DMBI$^+$-side chains interaction is positive, indicating a repulsive interaction. This yields a minimal total interaction energy of −106 kcal mol^{-1}, resulting in dopant cation instability.

To visually investigate the interactions between dopants and polymers, we extracted the representative conformations of the polymer-dopant pairs from MD simulations in the two systems and calculated the charge density and electrostatic potential maps (Figure S15, Supporting Information). In the P(TDPP-BT-LEG) system, the distance between the polymer and dopant is ≈6.8 Å, and the dopant interacts with both the polymer backbone and side chains, creating a larger area of electrostatic potential overlap. In contrast, in the P(TDPP-BT-C8C10) system, the distance is ≈9.1 Å, and the potential energy surface overlap between the dopant and the polymer backbone is minimal. Moreover, we found that in the P(TDPP-BT-C8C10) system, the dopants tend to intercalate within the side chains, further reducing the potential energy surface overlap and weakening the electrostatic interactions between the dopant and polymer.

Variations in side chains also lead to different dielectric environments, thereby affecting electrostatic interactions and charge transfer. To gain deeper insights, we performed DFT calculations to quantify energy changes associated with charge transfer between the TDPP-BT monomer and the TDAE dopant across different solvents with different dielectric constants (ε).[35,36] We employed implicit solvent models of ethylene glycol dimethyl ether (ε = 7.30) and n-hexane (ε = 1.88) to simulate dielectric environments analogous to EG side chains and alkyl side chains, respectively. Our investigation focused on charge transfer complex (CTC) formation and its subsequent separation into TDPP-BT$^-$ anion and TDAE$^+$ cation. Results showed that in the polar solvent, the Gibbs free energy of charge transfer was one-fourth the magnitude observed in *n*-hexane (Figure 3f), further validating that the polar environment, akin to that in the EG side-chain polymers, stabilizes the ionized products and enhances the dopant to polymer backbone electron/hydride transfer. Therefore, efficient n-doping, along with reduced structural and energetic disorder, enables polymers with EG side chains to achieve high conductivity.

2.3. Charge Transport Properties of P(TDPP-BT-LEG)

We adopted the Kang-Snyder model to analyze the *S*-σ relationship of the three LEG polymers (**Figure 4a**).[37] All polymers could be fitted by a transport exponent $s = 1$.[38] P(TDPP-BT-LEG) exhibits a transport coefficient (σ_{E0}) of 200 S cm^{-1}, 10 times higher than that of P(TDPP-BT2F-LEG) (σ_{E0} = 20 S cm^{-1}) and 20 times higher than that of P(TDPP-TQ-LEG) (σ_{E0} = 10 S cm^{-1}), indicating its intrinsically outstanding charge transport property. From the fitting, it is evident that at low carrier concentrations, P(TDPP-BT-LEG) consistently exhibits a larger *S*, consistent with a significantly large E_{Tr} and E_F gap. Therefore, we hypothesize that P(TDPP-BT-LEG) possesses an intrinsic large E_{Tr} and E_F gap, which implies that in its undoped state, its E_{Tr} and E_F gap are also larger. Temperature-dependent σ measurements at various doping ratios revealed a substantially larger hopping activation energy in P(TDPP-BT-LEG) (Figure 4b; Figure S16, Supporting Information). Particularly at lower doping concentrations, P(TDPP-BT-LEG) exhibits significantly elevated activation energy, further reflecting its intrinsic large energy gap between E_F and E_{Tr}.[12,39]

Since the backbone structure and planarity of P(TDPP-TQ-LEG) differ more significantly from those of the other two polymers (Figure S17, Supporting Information), we focused more on a comparative analysis of P(TDPP-BT-LEG) and P(TDPP-BT2F-LEG). Through X-ray photoelectron spectroscopy (XPS) and ultraviolet photoelectron spectroscopy (UPS), we derived charge carrier concentration (*n*) and quantified E_F shifts in both doped polymers. XPS spectra showed an *N*-DMBI$^+$ peak at 402 eV after doping, with intensity progressively increasing at higher doping concentrations (Figures S18 and S19, Supporting Information). This peak demonstrated significantly greater intensity in P(TDPP-BT2F-LEG), consistent with the absorption spectra. Charge carrier concentrations (*n*) were calculated from XPS data using integrated peak area ratios[40] (see Supplementary Information for more details). At equivalent doping concentration, P(TDPP-BT-LEG) exhibited lower *n* than P(TDPP-BT2F-LEG) (Figure 4c; Tables S5 and S6, Supporting Information). UPS analysis confirmed a progressive rise in E_F with increasing doping concentration. For identical doping levels, the E_F of P(TDPP-BT-LEG) shifts less significantly, agreeing well with the XPS results (Figure 4d,e). Therefore, the intrinsic large energy gap, along with the slow movement of the E_F, results in the high *S* of P(TDPP-BT-LEG) (Figure 4f).

Charge carrier mobilities (μ) for both polymers were calculated using the relation $\sigma = nq\mu$, where *q* is the elementary charge and *n* represents the charge carrier concentration obtained from XPS measurement.[40] Although its doping efficiency is low, P(TDPP-BT-LEG) exhibited higher μ at lower *n* (**Figure 5a**; Table S7, Supporting Information). We posit that the measured *n* overestimated the free carrier density in P(TDPP-BT-LEG) due to its higher hopping activation energy, resulting in an underestimated charge carrier mobility. As a result, we expect the mobility of doped P(TDPP-BT-LEG) to be higher. AC-Hall measurements also reflect that doped P(TDPP-BT-LEG) has higher mobility at the same doping level (Figure 5b; Table S8, Supporting Information). However, it should be emphasized that in materials dominated by hopping transport, the AC-Hall method tends to overestimate the carrier concentration and correspondingly underestimate the mobility due to partial screening by localized carriers.[41]

The surface morphologies and molecular stacking of undoped and doped polymer films were explored using atomic force microscopy (AFM) and grazing-incidence wide-angle X-ray scattering (GIWAXS). AFM analysis revealed that the morphologies of both polymers remain largely unchanged after

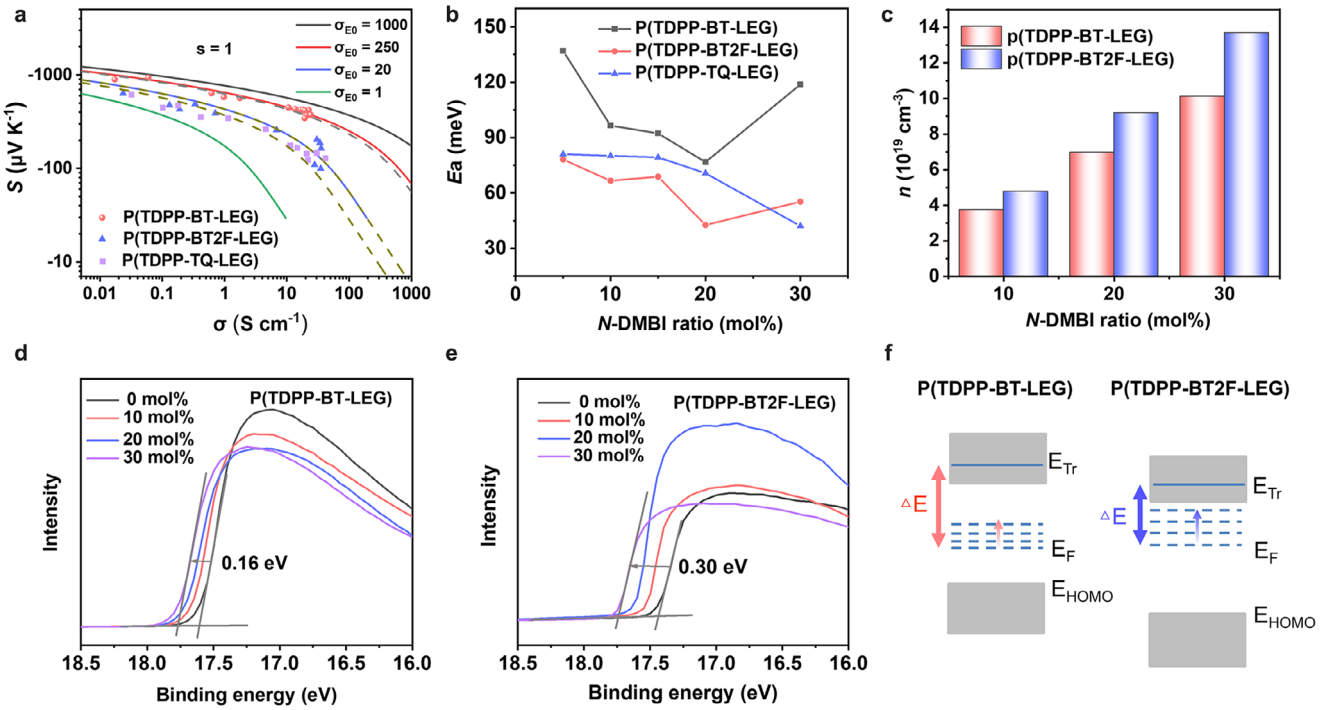

Figure 4. a) *S* vs σ plot for doped three LEG polymers with Kang-Snyder model fits. Solid curves: theoretical calculations using parameters shown; dashed line: global fit. b) Temperature-dependent electrical conductivities from 250 to 300 K of doped three LEG polymers at various *N*-DMBI doping ratios. c) Charge carrier concentrations of P(TDPP-BT-LEG) and P(TDPP-BT2F-LEG) films at varying doping levels, derived from XPS analysis. d,e) UPS spectra of the pristine and *N*-DMBI-doped polymers at different doping ratios. f) Schematic diagram of the energy level for pristine and doped polymers.

doping, indicating excellent miscibility between the dopants and polymer matrices (Figure 5c,d, Figures S20 and S21, Supporting Information). Notably, the P(TDPP-BT-LEG) film exhibits larger polymer aggregates, a structural feature conducive to enhanced charge transport.[42] GIWAXS results indicated a mixed face-on and edge-on orientation in P(TDPP-BT-LEG), establishing a 3D charge transport pathway[43,44] (Figure 5e–h; Figures S22 and S23, Supporting Information). Following *N*-DMBI doping, the lamellar spacing of P(TDPP-BT-LEG) remained unchanged, while the π–π stacking distances decreased from 3.60 to 3.58 Å (Table S9, Supporting Information). This suggested effective dopant incorporation without disrupting the crystalline framework, which was anticipated to enhance charge carrier mobility.[45] P(TDPP-BT2F-LEG) showed an edge-on orientation and reduced π–π stacking distances; however, its lamellar distance increased even after low-concentration doping. This indicated dopant penetration into the side-chain regions, which might disrupt ordered molecular packings and decrease charge transport.[45]

To further probe the intrinsic transport properties, we calculated intermolecular charge transfer integrals. Studies of conjugated polymers containing BT fragments demonstrate that strong BT-BT coupling could facilitate efficient intermolecular charge transport.[46–48] These polymers adopt varied packing orientations via acceptor-acceptor interactions, and the packing changes from parallel packing to perpendicular packing.[46] We calculated the charge transfer integrals (*J*) for TDPP-BT and TDPP-BT2F dimers across multiple crossing angles and stacking distances[46,48] (Figure S24, Supporting Information). The *J* values between acceptor units at various interchain crossing angles at π–π distances of 3.5 and 3.6 Å are shown in Figure 5i. For most packing angles, charge transfer integrals for BT-BT coupling exhibited higher values, indicating more efficient interchain charge transport through BT units. Crucially, at specific angles (e.g., 30°and 90°), there is a noticeable lack of LUMO orbital overlap between BT2F-BT2F, suggesting poor interchain electronic coupling (Figure 5j,k; Figure S25, Supporting Information). Consequently, the more efficient interchain charge transport pathway in P(TDPP-BT-LEG) contributes to its excellent charge transport properties, enabling the high electrical conductivity even at low charge carrier concentrations.

Statistical analysis of literature data revealed a correlation between thermoelectric properties and LUMO energy levels in n-type OTE materials (**Figure 6**; Table S10, Supporting Information): σ decreases with increasing LUMO level, while *S* trends upward. And we do not find a significant correlation between the *PF* and the LUMO energy. Therefore, we deduce that the evaluated LUMO level contributes to an intrinsically large transport-Fermi energy gap, which is crucial for achieving a high *S*. However, it also raises the barrier for dopant-to-polymer charge transfer, which negatively impacts σ. We demonstrated that introducing EG side chains could enhance electrostatic interactions between dopant cations and polymers, promoting charge transfer when the energy level condition is not fully met. Furthermore, efficient interchain couplings and preserved morphology in the doped film also greatly contribute to the high conductivity at low doping concentrations in P(TDPP-BT-LEG). These synergistic effects endow P(TDPP-BT-LEG) with superior thermoelectric

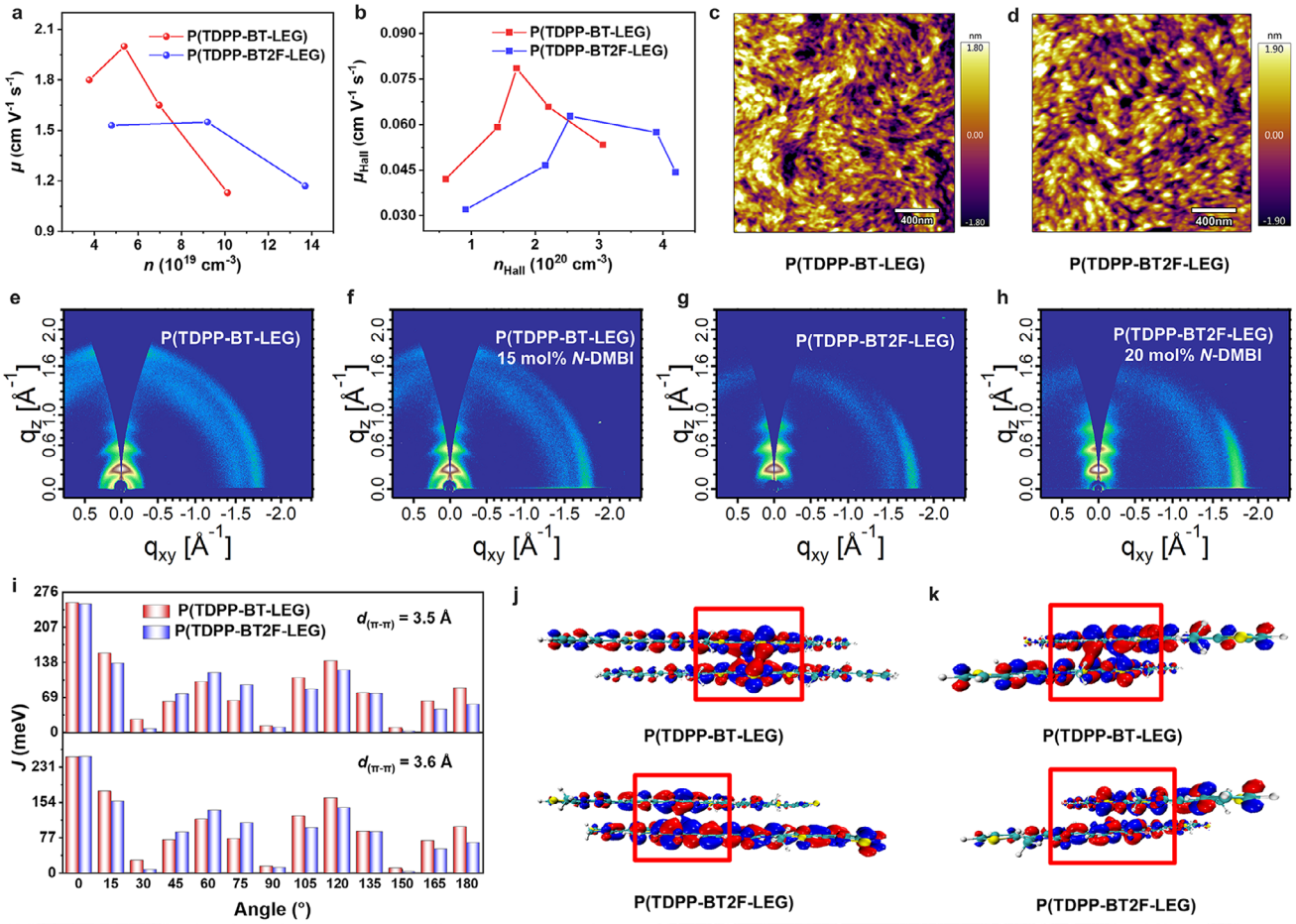

Figure 5. a) μ vs n plots for doped polymer films obtained from XPS measurements. b) μ vs n plot for doped polymer films obtained from the AC-Hall measurements. c,d) AFM height images of pristine (c) P(TDPP-BT-LEG) and (d) P(TDPP-BT2F-LEG) films. e–h) 2D GIWAXS patterns of (e&f) P(TDPP-BT-LEG) and (g&h) P(TDPP-BT2F-LEG) films under (left) pristine and (right) doped conditions. i) Computed transfer integrals between backbone units at varying interchain crossing angles with π–π distances of 3.5 Å (upper) and 3.6 Å (lower). j,k) Wave function overlap diagrams at (j) 30° and (k) 90° interchain angles (π–π distance: 3.6 Å).

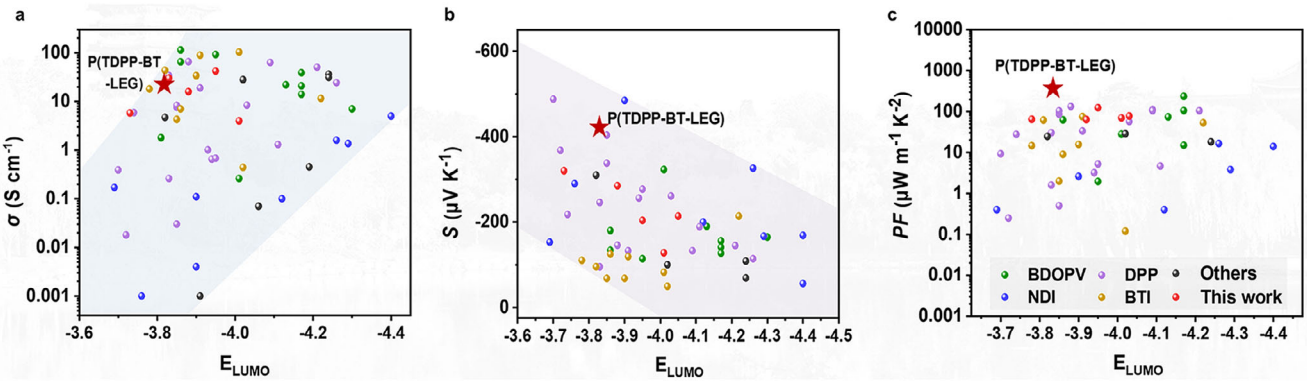

Figure 6. Statistical analysis of a) σ, b) S, and c) PF vs LUMO energy for n-doped polymers, including data from this study and literature. LUMO levels were determined or collected based on cyclic voltammetry (CV) results.

performance, achieving the highest PF and a high *ZT* among n-type conjugated polymer thermoelectric materials (Figure 6c; Table S10, Supporting Information).

Our current concern primarily revolves around the relatively high thermal conductivity of P(TDPP-BT-LEG), compared to other conjugated polymers, which may be linked to its strong chain entanglement and interchain interactions (see Supporting Information for details). In the future, we will explore blending P(TDPP-BT-LEG) with low thermal conductivity components or applying interface engineering techniques to reduce its thermal conductivity. Additionally, the ambient and thermal stability of P(TDPP-BT-LEG) remains insufficient. It can only maintain the excellent performance in an N_2 glovebox (Figure S26, Supporting Information). More work should focus on developing effective encapsulation methods that can minimize dedoping and ensure long-term reliability.

3. Conclusion

In summary, we have screened out a high-performance n-type thermoelectric polymer, p(TDPP-BT-LEG), featuring a high *S* at moderate σ, yielding a record-high n-type *PF*. This performance was attributed to three factors: 1) an intrinsically large transport-Fermi energy level, which enable a high *S*; 2) enhanced electrostatic interactions with dopant that mitigate the adverse effects of energy level misalignment on doping, thereby enabling effective polymer doping; and 3) efficient interchain coupling through BT units combined with preserved crystalline structure and morphology in the doped film, which collectively enabled high conductivity even at low charge carrier concentrations. This study provided valuable insights for synergistic polymer designs, including: energy level tuning to realize large *S*, underscoring the critical roles of EG side chains in enhancing electrostatic interactions and BT units in facilitating efficient charge transport.

Supporting Information

Supporting Information is available from the Wiley Online Library or from the author.

Acknowledgements

This work was supported by the National Natural Science Foundation of China (T2425010, T2521001 and 52403219). The authors acknowledge Molecular Materials and Nanofabrication Laboratory (MMNL) and Materials Processing and Analysis Center, Peking University, for the use of instruments. The computational part is supported by the High-Performance Computing Platform of Peking University. The authors acknowledge Prof. Chong-an Di and Dr. Dongyang Wang (Institute of Chemistry, Chinese Academy of Sciences) for their assistance with the thermal conductivity measurements.

Conflict of Interest

The authors declare no conflict of interest.

Author Contributions

J.W. and C.W. contributed equally to this work. C.W., Z.R., X.P., and J.C. synthesized the polymers. J.W., J.L., and J.W. performed device fabrication and characterization. J.W., C.W., S.T., and X.-Y.D. conducted the DFT and MD calculations. J.W., C.W., K.L., Z.Z., and T.L. wrote the manuscript. All the authors revised and approved the manuscript.

Data Availability Statement

The data that support the findings of this study are available from the corresponding author upon reasonable request.

Keywords

charge transport property, n-type conjugated polymers, organic thermoelectrics, Seebeck coefficients

Received: July 2, 2025
Revised: November 3, 2025
Published online: November 18, 2025

[1] S. Masoumi, S. O'Shaughnessy, A. Pakdel, *Nano Energy* **2022**, *92*, 106774.
[2] W. Liu, H. S. Kim, Q. Jie, Z. Ren, *Scr. Mater.* **2016**, *111*, 3.
[3] S. H. Wang, G. Z. Zuo, J. Kim, H. Sirringhaus, *Prog. Polym. Sci.* **2022**, *129*, 101548.
[4] W. Zhu, X. Qiu, J. E. M. Laulainen, H.-L. Un, X. Ren, M. Xiao, G. Freychet, P. Vacek, D. Tjhe, Q. He, W. Wood, Z. Wang, Y. Zhang, Z. Qu, J. Asatryan, J. Martin, M. Heeney, C. R. McNeill, P. A. Midgsley, I. E. Jacobs, H. Sirringhaus, *Adv. Mater.* **2024**, *36*, 2310480.
[5] H. Tang, Y. Liang, C. Liu, Z. Hu, Y. Deng, H. Guo, Z. Yu, A. Song, H. Zhao, D. Zhao, Y. Zhang, X. Guo, J. Pei, Y. Ma, Y. Cao, F. Huang, *Nature* **2022**, *611*, 271.
[6] D. Wang, J. Ding, Y. Ma, C. Xu, Z. Li, X. Zhang, Y. Zhao, Y. Zhao, Y. Di, L. Liu, X. Dai, Ye Zou, B. Kim, F. Zhang, Z. Liu, I. McCulloch, M. Lee, C. Chang, X. Yang, D. Wang, D. Zhang, L.-D. Zhao, C-A. Di, D. Zhu, *Nature* **2024**, *632*, 528.
[7] J. Ding, Z. Liu, W. Zhao, W. Jin, L. Xiang, Z. Wang, Y. Zeng, Y. Zou, F. Zhang, Y. Yi, Y. Diao, C. R. McNeill, C.-A. Di, D. Zhang, D. Zhu, *Angew. Chem., Int. Ed.* **2019**, *58*, 18994.
[8] Q. Yang, S. Yang, P. Qiu, L. Peng, T.-R. Wei, Z. Zhang, X. Shi, L. Chen, *Science* **2022**, *377*, 854.
[9] M. M Mallick, L. Franke, A. G. Rösch, H. Geßwein, Z. Long, Y. M. Eggeler, U. Lemmer, *Adv. Sci.* **2022**, *9*, 2202411.
[10] Y. Lu, Yi Zhou, Wu Wang, M. Hu, X. Huang, D. Mao, S. Huang, L. Xie, P. Lin, B. Jiang, B. Zhu, J. Feng, J. Shi, Q. Lou, Yi Huang, J. Yang, J. Li, G. Li, J. He, *Nat. Nanotechnol.* **2023**, *18*, 1281.
[11] X. Dai, Q. Meng, F. Zhang, Y. Zou, C. Di, D. Zhu, *J. Energy Chem.* **2021**, *62*, 204.
[12] K. Xu, T.-P. Ruoko, M. Shokrani, D. Scheunemann, H. Abdalla, H. Sun, C.-Y. Yang, Y. Puttisong, N B. Kolhe, J. S. M. Figueroa, J O. Pedersen, T. Ederth, W M. Chen, M. Berggren, S. A. Jenekhe, D. Fazzi, M. Kemerink, S. Fabiano, *Adv. Funct. Mater.* **2022**, *32*, 2112276.
[13] Z. Li, W. Fu, D. Scheunemann, X. Wei, M. Litterst, P. M. Viji, Y. Cui, J. Hou, J. Tang, Z. Liang, Z. Qu, M. Kemerink, R. Guo, G. Zuo, *Adv. Sci.* **2024**, *12*, 2409382.
[14] Z. Chen, Y. Wen, Y. Xu, D. Li, Q. Le, S. Shin, J. Ouyang, *Adv. Funct. Mater.* **2025**, *35*, 2424378.
[15] F. J. Zhang, C. Di, *Chem. Mater.* **2020**, *32*, 2688.
[16] G. Zuo, X. Liu, M. Fahlman, M. Kemerink, *Adv. Funct. Mater.* **2017**, *28*, 1703280.
[17] D. Wang, J. Ding, X. Dai, L. Xiang, D. Ye, Z. He, F. Zhang, S.-H. Jung, J.-K. Lee, C. Di, D. Zhu, *Adv. Mater.* **2023**, *35*, 2208215.
[18] X. Guan, J. Ouyang, *CCS Chem.* **2021**, *3*, 2415.

[19] C. Li, D. Luo, T. Wang, C. Shan, C. Li, K. Sun, A. K. K. Kyaw, J. Ouyang, *Small Struct.* **2023**, *4*, 2300245.
[20] S. D. Kang, G. J. Snyder, *Nat. Mater.* **2017**, *16*, 252.
[21] Y. Zou, D. Huang, Q. Meng, C. Di, D. Zhu, *Org. Electron.* **2018**, *56*, 125.
[22] X. Yan, M. Xiong, X.-Y. Deng, K.-K. Liu, J.-T. Li, X.-Q. Wang, S. Zhang, N. Prine, Z. Zhang, W. Huang, Y. Wang, J-Yu Wang, X. Gu, S. K. So, J. Zhu, T. Lei, *Nat. Commun.* **2021**, *12*, 5723.
[23] X.-X. Chen, J.-T. Li, Y.-H. Fang, X.-Y. Deng, X.-Q. Wang, G. Liu, Y. Wang, X. Gu, S.-D. Jiang, T. Lei, *Nat. Commun.* **2022**, *13*, 2258.
[24] H. Jia, Z. Huang, P. Li, S. Zhang, Y. Wang, J.-Y. Wang, X. Gu, T. Lei, *J. Mater. Chem. C* **2021**, *9*, 4927.
[25] J. Liu, B. van der Zee, R. Alessandri, S. Sami, J. Dong, M. I. Nugraha, A. J. Barker, S. Rousseva, L. Qiu, X. Qiu, N. Klasen, R. C. Chiechi, D. Baran, M. Caironi, T. D. Anthopoulos, G. Portale, R. W. A. Havenith, S. J. Marrink, J. C. Hummelen, L. J. A. Koster, *Nat. Commun.* **2020**, *11*, 5694.
[26] J. Liu, Li Qiu, R. Alessandri, X. Qiu, G. Portale, J. Dong, W. Talsma, G. Ye, A. A. Sengrian, P. C. T. Souza, M. A. Loi, R. C. Chiechi, S. J. Marrink, J. C. Hummelen, L. J. A. Koster, *Adv. Mater.* **2018**, *30*, 1704630.
[27] V. I. Arkhipov, P. Heremans, E. V. Emelianova, H. Bässler, *Phys. Rev. B* **2005**, *71*, 045214.
[28] C. Xu, D. Wang, *J. Mater. Chem. A* **2023**, *11*, 15416.
[29] M. Xiong, X.-Y. Deng, S.-Y. Tian, K.-K. Liu, Y.-H. Fang, J.-R. Wang, Y. Wang, G. Liu, J. Chen, D. R. Villalva, D. Baran, X. Gu, T. Lei, *Nat. Commun.* **2024**, *15*, 4972.
[30] S. E. Yoon, Y. Kang, J. Im, J. Lee, S. Y. Lee, J. Park, Y. J. Gao, D. Jeon, J. Y. Son, J. Kim, C. J. Kousseff, T. Kim, H. Seo, K. Kang, I. McCulloch, S. K. Kwak, H. H. Choi, B.-G. Kim, J. H. Kim, *Joule* **2023**, *7*, 2291.
[31] C.-Y. Yang, Y.-F. Ding, D. Huang, J. Wang, Z.-F. Yao, C.-X. Huang, Y. Lu, H.-I. Un, F.-D. Zhuang, J.-H. Dou, C.-A. Di, D. Zhu, J.-Y. Wang, T. Lei, J. Pei, *Nat. Commun.* **2020**, *11*, 3292.
[32] B. Honig, A. Nicholls, *Science* **1995**, *268*, 1144.
[33] T. A. Halgren, *J. Am. Chem. Soc.* **1992**, *114*, 7827.
[34] J. Liu, S. Maity, N. Roosloot, X. Qiu, Li Qiu, R C. Chiechi, J C. Hummelen, E. von Hauff, L. J. A. Koster, *Adv. Electron. Mater.* **2019**, *5*, 1800959.
[35] Y. Zeng, W. Zheng, Y. Guo, G. Han, Y. Yi, *J. Mater. Chem. A* **2020**, *8*, 8323.
[36] J. Han, C. Ganley, Q. Hu, X. Zhao, P. Clancy, T. P. Russell, H. E. Katz, *Adv. Funct. Mater.* **2021**, *31*, 2010567.
[37] S. A. Gregory, R. Hanus, A. Atassi, J. M. Rinehart, J. P. Wooding, A. K. Menon, M. D. Losego, G. J. Snyder, S. K. Yee, *Nat. Mater.* **2021**, *20*, 1414.
[38] Z.-D. Yu, Y. Lu, Z.-Y. Wang, H.-I. Un, S. J. Zelewski, Y. Cui, H.-Y. You, Y. Liu, K.-F. Xie, Z.-F. Yao, Y.-C. He, J.-Y. Wang, W.-B. Hu, H. Sirringhaus, J. Pei, *Sci. Adv.* **2023**, *9*, adf3495.
[39] A. von Mühlenen, N. Errien, M. Schaer, M.-N. Bussac, L. Zuppiroli, *Phys. Rev. B* **2007**, *75*, 115338.
[40] I. E. Jacobs, G. D'Avino, V. Lemaur, Y. Lin, Y. Huang, C. Chen, T. F. Harrelson, W. Wood, L. J. Spalek, T. Mustafa, C. A. O'Keefe, X. Ren, D. Simatos, D. Tjhe, M. Statz, J. W. Strzalka, J.-K. Lee, I. McCulloch, S. Fratini, D. Beljonne, H. Sirringhaus, *J. Am. Chem. Soc.* **2022**, *144*, 3005.
[41] H. T. Yi, Y. N. Gartstein, V. Podzorov, *Sci. Rep.* **2016**, *6*, 23650.
[42] C. Chen, H. Ma, K. Lu, X. Zhang, B. Yue, C. Song, P. Huang, H. Cheng, Y. Lin, *Adv. Mater.* **2025**, *37*, 2417594.
[43] J.-L. Li, X.-Y. Deng, J. Chen, P.-X. Fu, S.-Y. Tian, Y. Wang, X. Gu, T. Lei, *CCS Chem.* **2025**, *7*, 1449.
[44] Y. Zhang, D. Chang, Z. Wang, X. Lu, Y. Liu, Y. Zhao, *Adv. Mater.* **2025**, *37*, 2506041.
[45] A. Dash, S. Guchait, D. Scheunemann, V. Vijayakumar, N. Leclerc, M. Brinkmann, M. Kemerink, *Adv. Mater.* **2024**, *36*, 2311303.
[46] G. LeCroy, R. Ghosh, P. Sommerville, C. Burke, H. Makki, K. Rozylowicz, C. Cheng, M. Weber, W. Khelifi, N. Stingelin, A. Troisi, C. Luscombe, F. C. Spano, A. Salleo, *J. Am. Chem. Soc.* **2024**, *146*, 21778.
[47] H. Makki, C. Burke, A. Troisi, *ChemRxiv* **2023**, bt02b.
[48] J. F. Coker, S. Moro, A. S. Gertsen, X. Shi, D. Pearce, M. P. van der Schelling, Y. Xu, W. Zhang, J. W. Andreasen, C. R. Snyder, L. J. Richter, M. J. Bird, I. McCulloch, G. Costantini, J. M. Frost, J. Nelson, *Proc. Natl. Acad. Sci. USA* **2024**, *121*, 2403879121.